

# Mixing dynamics at river confluences governed by intermodal behaviour

Received: 22 April 2022

Accepted: 25 October 2022

Published online: 15 December 2022

 Check for updates

A. N. Sukhodolov<sup>1</sup>✉, O. O. Shumilova<sup>1</sup>, G. S. Constantinescu<sup>2</sup>, Q. W. Lewis<sup>3</sup>  
& B. L. Rhoads<sup>4</sup>

The extent to which flows mix at confluences is pivotal for determining spatial patterns of water quality and biodiversity. Because mixing processes are complex, predicting rates and characteristic scales of mixing is difficult. Here we introduce a theory for confluence mixing dynamics of shallow flows in which the mixing process is controlled by the switching between two modes of behaviour—one similar to a wake behind an obstacle and the other similar to a mixing layer between two parallel flows. Dye visualizations of mixing in field-based controlled experiments agree with theoretical predictions and support transitional behaviour between the two mixing modes. According to our theoretical framework, the mixing interface can grow rapidly in wake mode, when large vortices are shed from a zone of stagnant flow within the confluence, but lateral shear between incoming flows is negligible. This rapid growth occurs even though flow curvature and shallowness inhibit growth through advective and turbulent lateral exchange of momentum and through bed friction. Our findings provide insight into the importance of different modalities of flow structure in controlling mixing at river confluences, thereby contributing to practical knowledge on the role of confluences in dispersal of contaminants in river systems.

Waters of rivers flowing into confluences can create prominent visual patterns of mixing when the incoming flows differ in colour or turbidity. Such patterns provide visible evidence of abiotic processes that influence water quality and biodiversity in fluvial ecosystems<sup>1,2</sup> and define chemical transformations of transported substances downstream of confluences<sup>3,4</sup>. Complex patterns of turbulent flows associated with mixing also have important implications for channel morphology<sup>5–7</sup>, benthic fauna<sup>8,9</sup> and habitat use by fish<sup>10</sup>.

Contrasts in the turbidity of confluent rivers are often visible on widely available remote-sensing images<sup>11,12</sup>, and such contrasts provide the basis for identifying mixing interfaces characterized by interpenetration of highly turbid and less turbid waters (Fig. 1). In some instances, mixing interfaces are narrow near the junction apex and gradually

increase in width over distance (Fig. 1a). In other cases, the mixing interface originates downstream of a broad zone of stagnant water near the confluence apex and expands downstream rapidly (Fig. 1b).

Mixing along a mixing interface between incoming flows with different velocities has been a focus of field studies<sup>13–21</sup> and laboratory<sup>22–28</sup> and numerical<sup>29–33</sup> experiments, which have attempted to characterize this mixing using classic mixing-layer theory—a process of mixing referred to hereafter as mixing-layer mode<sup>34–37</sup>. Hydrodynamic theory<sup>34,35,37</sup> provides an asymptotic solution for this mode by relating the width of the mixing interface to the velocity difference between merging flows. When the velocity difference is small near the confluence apex, the theory<sup>37</sup> predicts that the layer should not grow. However, recent field and numerical studies show that, in contradiction

<sup>1</sup>Department of Ecohydrology and Biogeochemistry, Leibniz Institute of Freshwater Ecology and Inland Fisheries, Berlin, Germany. <sup>2</sup>Department of Civil and Environmental Engineering and IIHR Hydrosciences and Engineering, University of Iowa, Iowa City, IA, USA. <sup>3</sup>Department of Geography and Environmental Management, University of Waterloo, Waterloo, Ontario, Canada. <sup>4</sup>Department of Geography, University of Illinois at Urbana-Champaign, Champaign, IL, USA. ✉e-mail: [Alexander.Sukhodolov@igb-berlin.de](mailto:Alexander.Sukhodolov@igb-berlin.de)

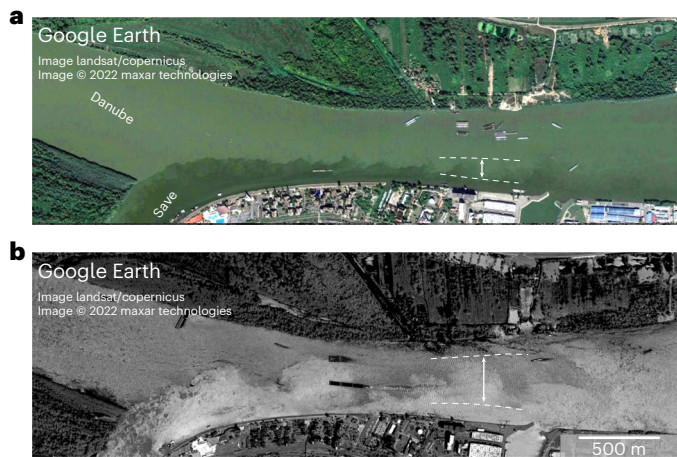


**Fig. 1 | Patterns of mixing at the confluence of the rivers Danube and Save at Belgrade, Serbia.** **a**, In the mixing-layer mode with higher momentum water from the Danube, 30 September 2017. **b**, In the wake mode, showing mixing of waters with almost equal momentum and turbulent vortices arranged into an unsteady wake pattern, 22 May 2014. Location: 44° 49' 54" N, 20° 26' 56" E. Credit: satellite images, Landsat/Copernicus, Google Earth © 2022 Maxar Technologies.

to classic mixing-layer theory, mixing interfaces for confluent flows with small velocity differences often grow rapidly over distance<sup>18,31,38,39</sup>. Constantinescu et al.<sup>39</sup> proposed a mode-switching hypothesis according to which the dynamics of mixing interfaces can change to a wake mode when the velocity difference between tributaries is small and the stagnation zone induces an internal velocity deficit that acts much like a wake behind an obstacle<sup>18,39–42</sup>. Although hydrodynamic theory provides an asymptotic solution for wakes<sup>37,40</sup>, a critical need exists for a theory-based model that can accommodate both mixing-layer and wake modes given that elements of these modes can potentially co-exist either at a confluence at different times or in different parts of a confluence at the same time. The development of such a model would also be valuable for providing predictions that could be evaluated by coupling ground-based monitoring and remote sensing of mixing over a broad range of spatial scales<sup>12</sup>.

In this Article, we introduce a theoretical framework for confluence mixing based on depth-averaged two-dimensional shallow-flow equations that include terms representing advective and turbulent fluxes of momentum as well as bed friction<sup>43</sup>. We show that lateral advective fluxes of momentum induced by helical motion driven by the planar geometry of confluences and by turbulence associated with lateral shear can greatly exceed the inhibiting effect of riverbed friction and thereby substantially enhance mixing at river confluences.

## Theoretical framework and experimental tests

The theoretical framework developed in this study is based on the mixing-length approach<sup>37</sup>, but in contrast to conventional use of single-velocity and length scales, we focus on the dynamics of mixing interfaces simultaneously controlled by multiple external and internal velocity and length scales. The difference in the mean velocities of the incoming tributaries,  $\Delta U_m$ , is the external velocity scale driving dynamics in the mixing-layer mode. The velocity deficit,  $\Delta U_w$ , induced by the stagnation zone near the confluence apex is an internal velocity scale related to differences in velocity between the stagnation zone and adjacent freestream flows; it drives the dynamics of a wake imbedded into the interface. Flow shallowness, the ratio of flow width ( $B$ ) to flow depth ( $H$ ), represents the stabilizing effect of bed friction. The converging planar morphology of a confluence is characterized by the junction angle  $\theta$ , which, in turn, is related to the radius of curvature  $R$  of the flows entering the confluence—an external length scale controlling lateral

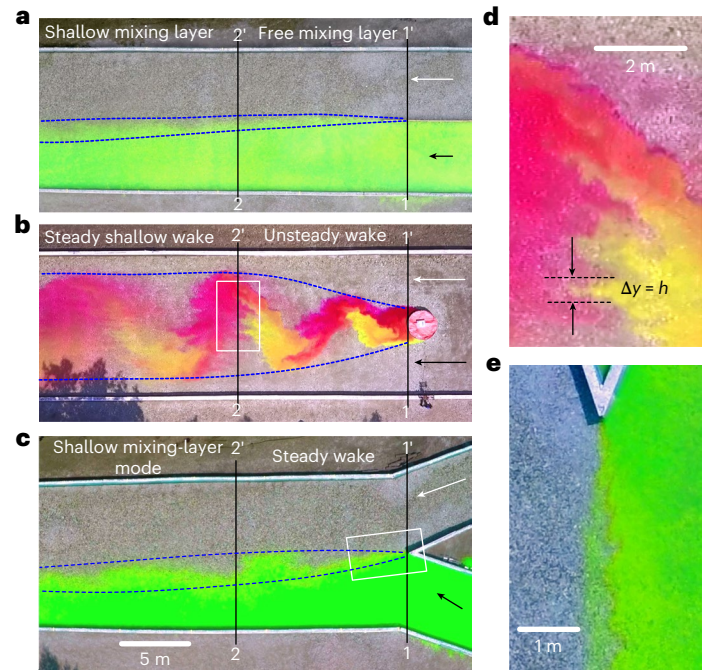


**Fig. 2 | Patterns of mixing in experiments.** **a**, Shallow mixing layer,  $M_f = 20$ . **b**, Shallow wake downstream of a circular obstruction with a diameter  $D = 2$  m (rectangle is enlarged in **d**). **c**, Shallow mixing interface at 40° confluence,  $M_f = 2.2$  (rectangle is enlarged in **e**). **d**, Patterns of large-scale lateral turbulence interacting with smaller-scale bed-friction-induced turbulence. Vertically oriented small vortices extract momentum from the large-scale lateral vortices and diffuse it in the ambient fluid through vortex stretching, which is visible through the feathering on edges of the large vortices. **e**, Pattern of mixing induced by streamwise-oriented vortical cells<sup>39</sup>. Lines 1–1' and 2–2' mark near-field boundaries; dashed lines are mixing-interface boundaries.

advective fluxes of momentum. Our theoretical framework accounts for interactions between these multiple scales to predict mixing-interface width  $\delta$ —the integral length scale of the mixing interface.

The theoretical model is derived by integrating the two-dimensional shallow-flow equations of momentum in a steady river flow with a realistic schematization of confluence geometry (Supplementary Fig. 1). Lateral advective fluxes of momentum are represented by parameterized solutions for the dynamic components of the total pressure head (Supplementary equation (7)) using the analogy of back-to-back curved flows within the confluence (Supplementary equation (13)). Alternatively, these fluxes can be represented as additional advective coefficients of friction for the wake stability parameter complementing bed friction<sup>41</sup> (Supplementary equation (9)). Because in river confluences advective fluxes greatly exceed turbulent fluxes<sup>18</sup>, they play a critical role in correct prediction of mixing.

Model predictions were tested using data obtained from field-based experiments. Most previous experimental research has examined flow structure in laboratory junctions with small  $B/H$  ratios and discordant channels<sup>5,23,24,27</sup>. Natural bed roughness and flow shallowness have not been previously considered in experimental contexts<sup>24,26–28</sup> but are recognized as crucial for theoretical modelling of shallow flows<sup>34–36,40</sup>. The lack of suitable experimental data necessitated completion of a set of controlled field experiments with  $B/H \geq 25$  and natural riverbed roughness (Fig. 2 and Extended Data Figs. 1, 4 and 6).

Experiments for shallow mixing layers ( $\Delta U_w = 0$ ) between parallel flows ( $R = 0$ ) and shallow wakes ( $\Delta U_m \approx 0$ ,  $R = 0$ ) in the lee of an obstacle allow rigorous testing of model predictions for interfaces with asymptotic behaviour, pure mixing-layer mode and pure wake mode (Fig. 2a,b and Supplementary Table 1). These experiments focus on the effects

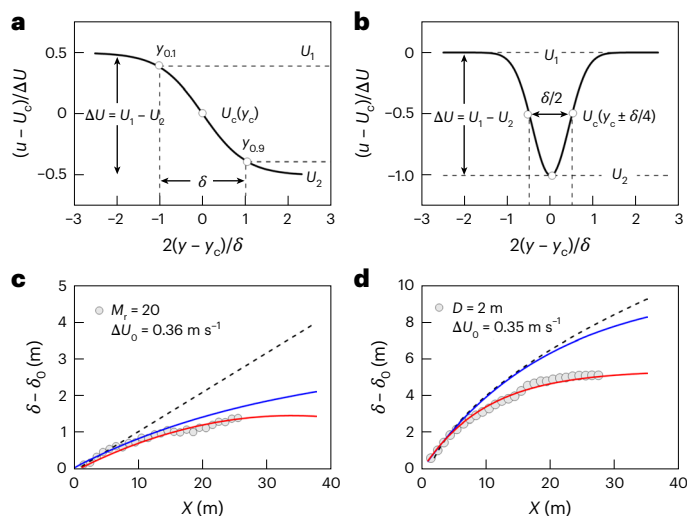


**Fig. 3 | Mixing interfaces with asymptotic behaviour: scales relations and comparison of predictions and measurements.** **a**, Mixing layer scaled by hyperbolic tangent function<sup>37</sup>. **b**, Wake scaled by exponential function<sup>37</sup>. **c**, Mixing in mixing-layer mode (splitter plate;  $M_r = 20$ ; dashed line is free mixing layer; solid lines are shallow mixing layer (blue, equation (7)), and accounting for lateral advection and turbulence (red, equation (6)). **d**, Mixing in wake mode (circular cylinder;  $M_r = 1$ ; dashed line is a free wake; solid lines are shallow wake, equation (7) with (red) and without (blue) the effects of lateral advection and turbulence).

on mixing of riverbed friction in shallow flows—a well-understood context for interpreting deviations from expected outcomes<sup>34,35,40</sup>. In the experiments with angled tributary channels ( $\theta = 40^\circ$  and  $70^\circ$ ,  $R > 0$ ), we explore the dynamics of mixing interfaces in the intermodal state ( $\Delta U_m, \Delta U_w \neq 0$ ) for a wide range of momentum flux ratio values  $2 \leq M_r \leq 100$ , where  $M_r = \rho_1 Q_1 U_1 / \rho_2 Q_2 U_2$ ,  $Q$  is the discharge,  $U$  is the flow velocity,  $\rho$  is the fluid density and subscripts 1 and 2 refer to each incoming flow<sup>42</sup> (Fig. 2c and Supplementary Table 1). The experimental measurements provide the basis for comparing theoretical predictions with documented outcomes and with shallow-flow theories<sup>34,35,40</sup> (Extended Data Figs. 3, 5a,c,d and 8c,d). The field-scale experiments are free of scaling effects present in most previous laboratory experiments<sup>22–28</sup> and, contrary to many field studies<sup>17,18,38,44</sup>, were obtained in true experiments, in which certain controls were kept nearly constant while others were varied.

### Asymptotic behaviour of a shallow mixing interface

Asymptotic behaviour for the theoretical framework corresponds to cases of free mixing layers and free wakes<sup>37</sup> and, by adding scales for shallowness<sup>34,35,40</sup>, links the asymptotes to the cases of shallow mixing layers (Fig. 3a) and shallow wakes (Fig. 3b). Predicted lateral profiles of depth-averaged streamwise velocity  $u(y)$ , where  $y$  is a lateral coordinate and  $U_c$  is the mean velocity in the mixing interface, match closely experimental data for the shallow mixing layer and shallow wake cases (Fig. 3a,b).

At short distances ( $x < 10$  m ( $x/H < 30$ , where  $x$  is a streamwise coordinate)), the mixing interface for the splitter-plate and wake experiments behaves as a free (deep) lateral shear flow, and experimental data collapse around the line of predicted values for such flows (dashed line) similar to findings of previous experimental<sup>34,35,37,40</sup> and field studies<sup>36</sup> (Fig. 3c,d and Extended Data Fig. 2). In both cases, the internal bed-generated boundary layer has not yet fully developed, and the effect of bed friction is minimal.

At long distances ( $x > 10$  m), the data systematically deviate from the prediction for free shear flows (Fig. 3c,d), which agrees with results

of previous studies<sup>33–35,40</sup> and with flow visualizations (Fig. 2c). Moreover, model predictions that account for the effects of bed friction only systematically overestimate rates of mixing (Fig. 3c,d). The full model, which includes the effects of lateral fluxes of momentum by advection and turbulence (Extended Data Fig. 9a,b), yields predictions that correspond closely to measured experimental data on mixing-interface growth (Fig. 3c,d). Lateral fluxes of momentum reduce rates of downstream growth by increasing the exchange of momentum between the confluent flows, thereby reducing the velocity difference between these flows (Extended Data Figs. 3c, 5c and 8c).

### Intermodal behaviour of mixing at angled confluences

Intermodal behaviour, or behaviour that includes mixing-layer and wake modes, is expected when a variety of scales substantially contribute to the dynamics of the mixing interfaces. In angled shallow confluences ( $R > 0$ ), the stagnation zone near the confluence apex<sup>17,45</sup> imposes a wake-like effect on the flow ( $\Delta U_m, \Delta U_w \neq 0$ ). To incorporate this effect into a multi-scale theoretical model, we introduce a lateral velocity profile in which the velocity scale  $\Delta U$  is a sum of mixing-layer  $\Delta U_m = \phi_m \Delta U$  and wake  $\Delta U_w = \phi_w \Delta U$  contributions ( $\phi_m + \phi_w = 1$ ). The shape of the composite velocity profile is determined by the ratio of external and internal velocity scales  $\varphi = \phi_m / \phi_w$  which provides a metric to characterize intermodal cases (Fig. 4a,b).

At short distances ( $x < 7$  m ( $x/H < 20$ )), the mixing interface behaves as a free wake, which exceeds, even for a momentum flux ratio of  $M_r \approx 5$ , the effect of the free mixing layer (Fig. 4c). For  $M_r = 2$ , the wake effect is quite strong, resulting in rapid initial growth of the mixing interface (Fig. 4d). Again, over these short distances from the junction apex, bed-friction effects are not pronounced (Extended Data Fig. 7). The predictions and patterns of experimental data also show how initial growth rates over distance associated with wake effects are much greater than those for the asymptotic mixing-layer case (Fig. 3c) and similar to those for the asymptotic wake case (Fig. 3d).

For  $x < 7$  m, the mixing interface evolves in a wake mode that depends on  $M_r$  (Fig. 4c,d). The switch from wake mode to mixing-layer mode occurs when the velocity deficit associated with the wake becomes small ( $\phi_w \approx 0$ ) and the mixing interface then behaves in a shallow mixing-layer mode. The distance from the apex at which this switch occurs determines whether the behaviour will be that of a free mixing layer or a shallow mixing layer, but in most cases it seems likely that this behaviour will be influenced to some extent by the stabilizing effects of lateral advective fluxes of momentum, turbulence and bed friction. Indeed, the experimental data conform well with predictions of the multi-scale model that includes these effects (Fig. 4c,d). Computation of the contributions of these different effects to exchange of momentum using data from the field experiments indicates that lateral advective fluxes contribute up to 70% of the exchange of momentum while only about 20% is contributed by bed friction—considerably less than previously indicated<sup>34,35,40</sup> (Extended Data Figs. 7, 9 and 10).

### Lateral advection and turbulence drive mixing at confluences

This study advances knowledge of the mixing process at river confluences by showing how this process can be understood theoretically and experimentally as consisting of two intrinsic modes of behaviour—wake mode and mixing-layer mode. We demonstrate that intermodal behaviour, involving switching from one mode of behaviour to the other, is the generic mechanism governing dynamics of the mixing interface at confluences. Moreover, advective effects, particularly those associated with streamline curvature caused by the angled planform geometry of confluences and the need for incoming flows to reorient in direction, play an important role in momentum exchange that drives these dynamics.

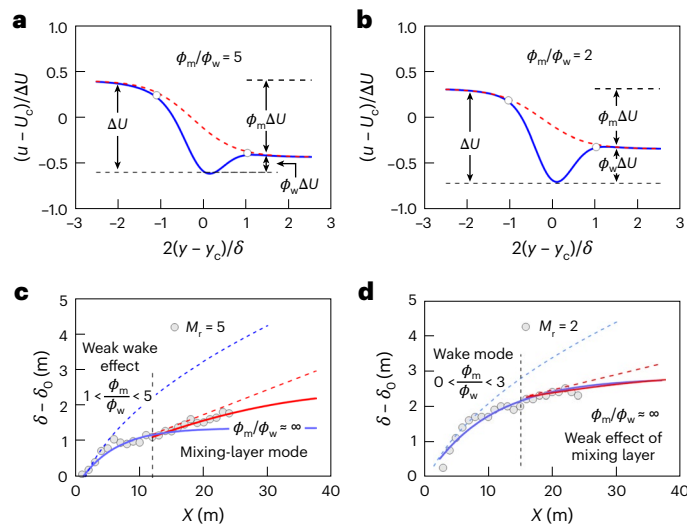


**Fig. 4 | Mixing interface with intermodal behaviour: scale relations and comparison of predictions and measurements.** **a**, In mixing-layer mode with a small wake effect (solid blue line is equation (8); dashed line is hyperbolic tangent function<sup>37</sup>). **b**, In wake mode with a small mixing-layer effect. **c**, Mixing with a weak wake effect ( $40^\circ$ ,  $M_r = 5$ ; solid red line is equation (6), red dashed line is free mixing layer, solid blue line is equation (7) and dashed blue line is free wake). **d**, Mixing with a weak mixing-layer effect ( $40^\circ$ ,  $M_r = 2$ , the same definitions for lines as in c).

The study provides the theoretical framework that consistently addresses findings of field research and numerical modelling of natural confluences, which has emphasized strong wake-like flow associated with flow stagnation and has shown that advective lateral fluxes of momentum can greatly exceed effects of shear-driven turbulence and bed friction<sup>18,36,41</sup> (Extended Data Fig. 9). By incorporating a metric that accounts for wake and mixing-layer effects on the transverse pattern of depth-averaged velocity within a confluence, our theoretical approach introduces a schematization that couples the effects of momentum ratio with wake effects, thereby accommodating a mode-switching mechanism to account for a wide range of intermodal growth dynamics of the mixing interface. The study shows clearly that treating confluence flows as similar to flow downstream of a thin splitter plate separating parallel flows<sup>34–36</sup> is overly simplistic because it does not consider the effects of flow stagnation and curvature within confluences.

For testing of our theoretical model, we draw on a dataset obtained in field experiments. These experiments examined the asymptotic and intermodal behaviour of the mixing interface in a shallow ( $B/H > 25$ ), hydraulically rough open-channel Y-shaped confluence with a naturally formed gravel bed ( $H/d_{50} = 17$ ) in a wide range of momentum ratios ( $2 < M_r < 100$ ) for three junction angles ( $0^\circ$ ,  $40^\circ$  and  $70^\circ$ ). Comparison of theoretical predictions with the results of field-based experiments shows that dynamics of mixing interface modelled using only bed friction systematically underestimate the stabilization effects related to lateral advective and turbulent fluxes of momentum—effects that are accommodated within our model (Fig. 3).

Comparison of experimental data with theoretical predictions shows that accounting for mode-switching mechanism together with the correct representation of lateral advective and turbulent fluxes of momentum provides accurate prediction of mixing with fast and slow rates (Fig. 4). These findings agree with the results reported for a large shallow river<sup>19</sup> ( $B/H \approx 470$ ) that a fast rate of mixing ( $M_r = 1.8$ ) is attributed to the development of channel-scale lateral circulation that was not observed at a slow mixing rate ( $M_r = 3.6$ ). The results agree also with studies on small rivers<sup>15,17,21</sup> reporting faster mixing than would be expected from conventional transverse diffusion models<sup>14,46</sup> that relate

transverse mixing distance  $L_y \approx 0.18UB^2/K$  to the effect of bed friction alone (for example,  $K = 0.42HU_*$ , where  $K$  is the dispersion coefficient and  $U_*$  is the shear velocity).

The theoretical framework highlights the value of near-field processes in the vicinity of the confluence apex on the mixing in the far field because at short distances the wake sets the initial width of the interface in a weak mixing-layer mode (Fig. 4c,d). Although the stagnation zone has been recognized as an important element in conceptual models<sup>6,22,45,47</sup>, it remains comparatively less studied, and our work suggests that understanding of stagnation-zone hydrodynamics can substantially improve predictions of mixing. Furthermore, our theoretical framework provides promising opportunities for predicting rates of mixing from remotely sensed images and should enhance capabilities to analyse mixing on the basis of geographical information systems<sup>12</sup>.

Although our theoretical framework captures many relevant aspects of mixing, additional factors require further experimental and theoretical assessment. Past work has shown that flow at confluences may not be characterized only by wake and mixing-layer behaviour<sup>18</sup> but also by jet-like behaviour<sup>44</sup>, which may be especially pronounced in confluences with discordant beds<sup>15,16,23</sup>. Cross-flow driven by density differences may also be important where incoming flows differ greatly in temperature, salinity or suspended load<sup>20,48</sup>. Unravelling the importance of these additional effects requires a firm understanding of how advective and diffusive processes affect mixing under less complicated conditions, and the present study sheds new light on how mixing occurs under such conditions.

## Online content

Any methods, additional references, Nature Portfolio reporting summaries, source data, extended data, supplementary information, acknowledgements, peer review information; details of author contributions and competing interests; and statements of data and code availability are available at <https://doi.org/10.1038/s41561-022-01091-1>.

## References

- Grant, E. H. C., Lowe, W. H. & Fagan, W. F. Living in branches: population dynamics and ecological processes in dendritic networks. *Ecol. Lett.* **10**, 165–175 (2007).
- Rice, S. P., Ferguson, R. I. & Hoey, T. B. Tributary control of physical heterogeneity and biological diversity at river confluences. *Can. J. Fish. Aquat. Sci.* **63**, 2553–2566 (2006).
- Schemel, L. E., Kimball, B. A., Runkel, R. L. & Cox, M. H. Formation of mixed Al–Fe colloidal sorbent and dissolved-colloidal partitioning of Cu and Zn in the Cement Creek–Animas River confluence, Silverton, Colorado. *Appl. Geochem.* **22**, 1467–1484 (2007).
- Bouchez, J. et al. Turbulent mixing in the Amazon River: the isotopic memory of confluences. *Earth Planet. Sci. Lett.* **290**, 37–43 (2010).
- Best, J. L. Sediment transport and bed morphology at river confluences. *Sedimentology* **35**, 481–498 (1988).
- Paola, C. When streams collide. *Nature* **387**, 232–233 (1997).
- Guillen-Ludena, S., Cheng, Z., Constantinescu, G. & Franca, M. J. Hydrodynamics of mountain–river confluences and its relationship to sediment transport. *J. Geophys. Res. Earth Surf.* **122**, 901–924 (2017).
- Rice, S. P., Greenwood, M. T. & Joyce, C. B. Tributaries, sediments sources, and longitudinal organization of macro-invertebrate fauna along river systems. *Can. J. Fish. Aquat. Sci.* **58**, 824–840 (2001).
- Blettler, M. C. M. et al. The impact of significant input of fine sediment on benthic fauna at tributary junctions: a case study of the Bermejo–Paraguay river confluence, Argentina. *Ecohydrol.* **8**, 340–352 (2015).

10. Scholz, A. T., Horrall, R. M., Cooper, J. C. & Hasler, A. D. Imprinting to chemical cues: the basis for home stream selection in salmon. *Science* **192**, 1247–1249 (1976).
11. Piegay, H. et al. Remotely sensed rivers in the Anthropocene: state of the art and prospects. *Earth Surf. Process. Landf.* **45**, 157–188 (2020).
12. Umar, M., Rhoads, B. L. & Greenberg, J. A. Use of multispectral satellite remote sensing to assess mixing of suspended sediment downstream of large river confluences. *J. Hydrol.* **556**, 325–338 (2018).
13. MacKay, J. R. Lateral mixing of the Liard and Mackenzie rivers downstream from their confluence. *Can. J. Earth Sci.* **7**, 111–124 (1970).
14. Fischer, H. B., List, E. J., Kom, R. C. Y., Imberger, J. & Brooks, N. H. *Mixing in Inland and Coastal Waters* (Academic Press, 1979).
15. Gaudet, J. M. & Roy, A. G. Effect of bed morphology on flow mixing length at river confluences. *Nature* **373**, 138–139 (1995).
16. De Serres, B., Roy, A. G., Biron, P. M. & Best, J. L. Three-dimensional structure of flow at a confluence of river channels with discordant beds. *Geomorphology* **26**, 313–335 (1999).
17. Rhoads, B. L. & Sukhodolov, A. N. Field investigation of three-dimensional flow structure at stream confluences 1. Thermal mixing and time-averaged velocities. *Water Resour. Res.* **37**, 2393–2410 (2001).
18. Rhoads, B. L. & Sukhodolov, A. N. Lateral momentum flux and the spatial evolution of flow within a confluence mixing interface. *Water Resour. Res.* **44**, W08440 (2008).
19. Lane, S. N. et al. Causes of rapid mixing at a junction of two large rivers: Rio Parana and Rio Paraguay, Argentina. *J. Geophys. Res.* **113**, F02019 (2008).
20. Laraque, A., Guyot, J. L. & Filizola, N. Mixing processes in the Amazon River at the confluences of the Negro and Solimoes rivers, Encontro das Aguas, Manaus, Brazil. *Hydrol. Proc.* **23**, 3131–3140 (2009).
21. Lewis, Q. W. & Rhoads, B. L. Rates and patterns of thermal mixing at a small stream confluence under variable incoming flow conditions. *Hydrol. Process.* **29**, 4442–4456 (2015).
22. Mosley, M. P. An experimental study of channel confluences. *J. Geol.* **84**, 535–562 (1976).
23. Best, J. L. & Roy, A. G. Mixing-layer distortion at the confluence of channels of different depth. *Nature* **350**, 411–413 (1991).
24. Biron, P., Roy, A. G. & Best, J. L. Turbulent flow structure at concordant and discordant open-channel confluences. *Exp. Fluids* **21**, 437–446 (1996).
25. Weber, L. J., Schumate, E. D. & Mawer, N. Experiments on flow at a 90° open-channel junction. *J. Hydraul. Eng.* **127**, 340–350 (2001).
26. Ribeiro, M. L., Blanckaert, K., Roy, A. G. & Schleiss, A. J. Hydromorphological implications of local tributary widening for river rehabilitation. *Water Resour. Res.* **48**, W10528 (2012).
27. Herrero, H. S., Garcia, C. M., Pedocchi, F., Lopez, G. & Szupiany, R. N. Flow structure at confluence: experimental data and bluff body analogy. *J. Hydraul. Res.* **54**, 263–274 (2016).
28. Birjukova Canelas, O., Ferreira, R. M. L., Guillen-Ludena, S., Alegria, F. C. & Cardoso, A. H. Three dimensional flow structure at fixed 70° open-channel confluence with bed discordance. *J. Hydraul. Res.* **58**, 434–446 (2020).
29. Bradbrook, K. F., Lane, S. N. & Richards, K. S. Numerical simulation of three-dimensional, time-averaged flow structure at river confluences. *Water Resour. Res.* **36**, 2731–2746 (2000).
30. Biron, P. M., Ramamurthy, A. S. & Han, S. Three-dimensional numerical modeling of mixing at river confluences. *J. Hydraul. Eng.* **130**, 243–253 (2004).
31. Constantinescu, G., Miyawaki, S., Rhoads, B. & Sukhodolov, A. Numerical analysis of the effect of momentum ratio on the dynamics and sediment-entrainment capacity of coherent flow structures at a stream confluence. *J. Geophys. Res.* **117**, F04028 (2012).
32. Constantinescu, G., Miyawaki, S., Rhoads, B. L. & Sukhodolov, A. N. Influence of planform geometry and momentum ratio on thermal mixing at a stream confluence with a concordant bed. *Environ. Fluid Mech.* **16**, 845–873 (2016).
33. Cheng, Z. & Constantinescu, G. Shallow mixing layers between non-parallel streams in a flat-bed, wide channel. *J. Fluid Mech.* **916**, A41 (2021).
34. Chu, V. H. & Babarutsi, S. Confinement and bed-friction effects in shallow turbulent mixing layers. *J. Hydraul. Eng.* **114**, 1257–1274 (1988).
35. Uijtewaal, W. S. J. & Booij, R. Effects of shallowness on the development of free-surface mixing layers. *Phys. Fluids* **12**, 392–402 (2000).
36. Sukhodolov, A., Schnauder, I. & Uijtewaal, W. Dynamics of shallow lateral shear layers: experimental study in a river with a sandy bed. *Water Resour. Res.* **46**, W11519 (2010).
37. Pope, S. B. *Turbulent Flows* (Cambridge Univ. Press, 2000).
38. Sukhodolov, A. N. & Rhoads, B. L. Field investigation of three-dimensional flow structure at stream confluences 2. Turbulence. *Water Resour. Res.* **37**, 2411–2424 (2001).
39. Constantinescu, G., Miyawaki, S., Rhoads, B., Sukhodolov, A. & Kirkil, G. Structure of turbulent flow at a river confluence with momentum and velocity ratios close to 1: insight provided by eddy-resolving numerical simulation. *Water Resour. Res.* **47**, W05507 (2011).
40. Chen, D. & Jirka, G. H. Experimental study of plane turbulent wakes in shallow water layer. *Fluid Dyn. Res.* **16**, 11–41 (1995).
41. Sukhodolov, A. N. & Sukhodolova, T. A. Shallow wake behind exposed wood-induced bar in a gravel-bed river. *Environ. Fluid Mech.* **14**, 1071–1083 (2014).
42. Rhoads, B. L. *River Dynamics: Geomorphology to Support Management* (Cambridge Univ. Press, 2020).
43. Nezu, I. & Nakagawa, H. *Turbulence in Open-Channel Flows* (A.A. Balkema, 1993).
44. Sukhodolov, A. et al. Turbulent flow structure at a discordant river confluence: asymmetric jet dynamics with implications for channel morphology. *J. Geophys. Res. Earth Surf.* **122**, 1278–1293 (2017).
45. Best, J. L. in *Recent Developments in Fluvial Sedimentology* (eds Etheridge, F. G. et al.) 27–35 (SEPM, 1987).
46. Rutherford, J. C. *River Mixing* (John Wiley & Sons, 1994).
47. Ashmore, P. E., Ferguson, R. I., Prestegard, K. L., Ashworth, P. J. & Paola, C. Secondary flow in anabranch confluences of a braided, gravel-bed stream. *Earth Surf. Process. Landf.* **17**, 299–311 (1992).
48. Horna-Munoz, D., Constantinescu, G., Rhoads, B., Lewis, Q. & Sukhodolov, A. Density effects at a concordant bed natural river confluence. *Water Resour. Res.* **56**, e2019WR026217 (2020).

**Publisher's note** Springer Nature remains neutral with regard to jurisdictional claims in published maps and institutional affiliations.

**Open Access** This article is licensed under a Creative Commons Attribution 4.0 International License, which permits use, sharing, adaptation, distribution and reproduction in any medium or format, as long as you give appropriate credit to the original author(s) and the source, provide a link to the Creative Commons license, and indicate if changes were made. The images or other third party material in this article are included in the article's Creative Commons license, unless indicated otherwise in a credit line to the material. If material is not included in the article's Creative Commons license and your intended use is not permitted by statutory regulation or exceeds the permitted use, you will need to obtain permission directly from the copyright holder. To view a copy of this license, visit <http://creativecommons.org/licenses/by/4.0/>.

© The Author(s) 2022

## Methods

We consider that the two confluent flows are shallow ( $B/H > 10$ ), concordant and steady. Theoretical analysis focuses on the post-junction shallow flow ( $B/H > 20$ ) downstream of the junction apex (Fig. 2a–c, lines 1–1). The coordinate system consists of a streamwise axis  $x$  with the origin at the downstream edge of a junction apex, a lateral coordinate  $y$  with the origin at the centreline and a vertical coordinate  $z$  with the origin at the riverbed and directed upwards.

Following the mixing-length approach, the dynamics of the mixing interface are modelled as<sup>37</sup>

$$\frac{d\delta}{dx} = \alpha \frac{\Delta U}{U_c}, \quad (1)$$

where  $\alpha$  is the spreading coefficient. The average values of the spreading coefficient are 0.11<sup>35–37</sup> in free (for example, away from boundaries/deep flow) mixing layers and 0.08 in a plane wake of a cylinder<sup>37</sup>.

A single-scale approach assumes that the velocity differential is constant along the mixing layer ( $\Delta U/U_c = \text{const}$ ) and that it decays over the distance in a plane wake as  $\Delta U/U_c \approx x^{-1/2}$ . Integration of equation (1) yields a linear growth of  $\delta \approx x$  for free mixing layers and  $\delta \approx x^{1/2}$  for free plane wakes.

In mixing interfaces affected by multiple processes and scales, the velocity differential changes due to additional exchange of momentum caused by external (flow curvature) and internal (riverbed roughness) processes and scales. This exchange of momentum directly affects the dynamics of the mixing interface. Specifically in shallow flows, the growth of the mixing interface is suppressed by friction on a solid boundary<sup>34,35,40</sup>.

Two velocity difference functions are obtained by integrating the two-dimensional shallow-water equations (Supplementary equations (1–9))

$$\Delta U = \Delta U_0 - \beta x, \quad \text{and} \quad (2)$$

$$\Delta U = \Delta U_0 \exp(-\lambda x), \quad (3)$$

where  $\beta$  and  $\lambda$  are decay rates of velocity difference and  $\Delta U_0 = \Delta U(x=0)$ . In our multi-scale theoretical framework, the velocity decay rates are functions of flow bathymetry, curvature and bed friction. In the theory of shallow flows<sup>34,35,40</sup>, the effects of flow bathymetry and curvature are neglected, and conventionally, only equation (3) is used with  $\lambda$  representing bed friction as

$$\lambda = c_f/H \quad (4)$$

in shallow mixing layer<sup>35,36</sup>, and

$$\lambda = 0.5 C_w/D \quad (5)$$

in shallow wake<sup>40</sup>, where  $c_f$  is the bed-friction factor,  $C_w$  is the wake stability parameter and  $D$  is the diameter of the obstacle producing wake. The wake stability parameter is also obtained for shallow wakes considering only bed friction<sup>40</sup>. In our study, we demonstrate that in equations (2)–(5), the decay rates  $\lambda$  should be calculated using the total resistance factor  $c_r$ , which includes contributions of lateral advective and turbulent fluxes of momentum, bed friction and pressure difference terms (Supplementary equation (9)).

Although equations (2) and (3) describe the same processes, their integration yields different solutions for the mixing interface width

$$\delta(x) = \alpha \frac{\Delta U_0}{U_c} x \left( 1 - \frac{\beta}{2\Delta U_0} x \right) + \delta_0, \quad (6)$$

and

$$\delta(x) = \alpha \frac{\Delta U_0}{U_c} \lambda^{-1} (1 - \exp(-\lambda x)) + \delta_0, \quad (7)$$

where  $\delta_0$  is the initial thickness of the mixing interface and the constant of integration. These two equations generally provide the same solutions for certain flow conditions, but their specific use can have some advantages and disadvantages. The parabolic solution (equation (6)) predicts both growth and decay of the mixing interface when velocity difference becomes small, while the exponential function (equation (7)) predicts only asymptotic infinite growth of the mixing interface. This difference has important implications for predicting mixing far away from the confluence and predictions of complete mixing. Equation (2) can also predict an increase of velocity difference where the river bottom is steeply sloping, as for example at discordant confluences. However, the consideration of such cases is beyond the scope of the present study. Equation (7) has the advantage that it universally applies to the mixing interface in both mixing-layer and wake modes, and the change of mode requires only a change in parameters (Fig. 4c,d). Furthermore, parameterization of  $\lambda$  in our model provides a theoretical background for previous empirical classification of shallow wakes<sup>40</sup>. This classification shows that a shallow wake behaves as (1) vortex street for  $C_w < 0.2$ , (2) unsteady wake for  $0.2 < C_w < 0.5$  and (3) steady wake for  $C_w > 0.5$ . We demonstrate that  $C_w$  increases with increasing lateral advective and turbulent fluxes of momentum (Extended Data Fig. 9a–c).

For intermodal behaviour of the mixing interface, we propose a semi-empirical model for a lateral depth-averaged profile of mean streamwise velocity

$$\frac{u - U_c}{\Delta U} = \frac{1}{2} \phi_m \tanh \zeta - \phi_w^{1/2} \exp(-4 \ln 2 \zeta^2), \quad \phi_m + \phi_w = 1, \quad \xi = 2(y - y_c)/\delta, \quad (8)$$

which is based on hyperbolic tangent and exponential solutions of mixing layers and wakes<sup>37</sup>. Equation (8) assumes that the wake is imbedded into the mixing layer with external velocities matching velocities of merging tributaries and that the velocity difference is composed of mixing-layer mode and wake contributions (Fig. 4a,b). Comparison of equation (8) with measured profiles in our experimental studies shows a good agreement (Extended Data Fig. 8a,b).

The field experiments reported in this study were completed in a side branch of the Tagliamento River in northeastern Italy in a relatively straight and shallow part of the channel located at 46° 12' 9.45" N, 12° 58' 14.55" E. This river reach is characterized by a stable hydraulic regime during the summer period when the flow is 30–40 cm deep and 25–30 m wide. Bed material, which is mostly immobile during summer, ranges from medium ( $d_{16} = 14$  mm) to coarse ( $d_{84} = 38.7$  mm) gravel with  $d_{50} = 22.5$  mm. Experiments with shallow mixing layers and angled confluences were carried out during June–August 2015<sup>49</sup>. The study of shallow wakes was performed during June–September 2019<sup>50</sup>. In the experiments with shallow mixing layers and shallow wakes, straight 40 and 50 m long and 10 m wide rectangular in-stream flumes were built in the central part of the side branch (Supplementary Table 1). The models of angled confluences consisted of symmetrical Y-shaped junctions with 5 m wide and 10 m long tributary channels. Experiments were conducted for models with junction angles of 0°, 40° and 70° with  $M_f$  ranging from 2 to 100 (Supplementary Table 1). Confluence angles of 45° are characteristic of natural junctions in arid landscapes while 72° angles are typical of junctions in humid environments<sup>42</sup>.

The experimental programme consisted of detailed measurements of the instantaneous flow velocities, topography of the free surface and visualization of flow patterns. Velocity measurements were performed with arrays of five (mixing layers) to seven (wakes) acoustic Doppler velocimeters (Vectrino+, Nortek AS). Surveys of

the free surface topography were carried out with a laser total station Elta 55 (Zeiss). Visualizations of flow patterns were performed using uranine (green) and rhodamine (red) dyes (Fig. 2) and recorded with Phantom II and Mavic Pro quadcopters. Velocities were collected at sampling frequencies of 10 and 25 Hz during the periods of 240 s on high-resolution spatial mesh of sampling locations (10–28 lateral transects with 10–14 sampling locations). Topographical surveys of the free surface were completed at short ranges (less than 30 m), enabling the vertical precision of elevation measurements within 1 mm. Visual patterns of dye tracers were recorded at the altitude of 40 m with a resolution of  $2,704 \times 1,520$  pixels per frame at a rate of 25 frames per second for a period of about 10 min. Post-processing of velocity measurements was performed with the software package ExploreV (Nortek AS). The topographical surveys were post-processed to obtain the spatial maps of free surface topography. Post-processing of video records included rectification of images and geo-referencing to the local system of coordinates using the benchmarks on the walls of in-stream flumes. Further detailed information on the experiments and data post-processing is available from our recent publications<sup>49,50</sup>.

## Data Availability

The database of shallow mixing layers and angled confluences study can be accessed in the public repository Open Source Framework (<https://osf.io/9f2uv>). Data on experiments with shallow wakes are available with open access via the Zenodo portal (<https://doi.org/10.5281/zenodo.3968748>). The field experiments were digitally recorded, and video documentaries are publicly accessible at <https://youtu.be/5wXjvzqxONI>, <https://youtu.be/gM-Zr-rhflY> and <https://youtu.be/Fe9KER33Pc4>. Source data are provided with this paper.

## References

49. Sukhodolov, A. N. & Sukhodolova, T. A. Dynamics of flow at concordant gravel bed river confluences: effects of junction angle and momentum flux ratio. *J. Geoph. Res. Earth Surf.* **124**, 588–615 (2019).
50. Shumilova, O. O., Sukhodolov, A. N., Constantinescu, G. S. & MacVicar, B. J. Dynamics of shallow wakes on gravel-bed floodplains: dataset from field experiments. *Earth Syst. Sci. Data* **13**, 1519–1529 (2021).

## Acknowledgements

T. Sukhodolova, A. Sukhodolova and T. Brosinski are thanked for the help with the field measurements. This research was done using the research platform RIVER LAB of IGB and financial support

by the grants SU 405/7-1 and SU 405/10-1 from the Deutsche Forschungsgemeinschaft (DFG, German Research Foundation). This project has also received funding from the European Union's Horizon 2020 research and innovation programme under the Marie Skłodowska-Curie grant agreement no. 860800.

## Author contributions

A.N.S. designed and participated in all experimental fieldwork and post-processed and analysed the results. A.N.S. performed analytical modelling and wrote and revised the manuscript in accordance with the suggestions of other authors. O.O.S. assisted in the experiments with shallow wakes, performed post-processing, analysis of the results and editing of the manuscript. B.L.R. and Q.W.L. participated in the experiments with angled confluences and provided valuable discussions and revisions of the manuscript at different stages of production. G.S.C. provided significant scientific input at different stages related to planning of the study and analysis of its results. G.S.C. is also credited with insightful discussions and detailed revisions of the manuscript.

## Funding

Open access funding provided by Leibniz-Institut für Gewässerökologie und Binnenfischerei (IGB) im Forschungsverbund Berlin e.V..

## Competing interests

The authors declare no competing interests.

## Additional information

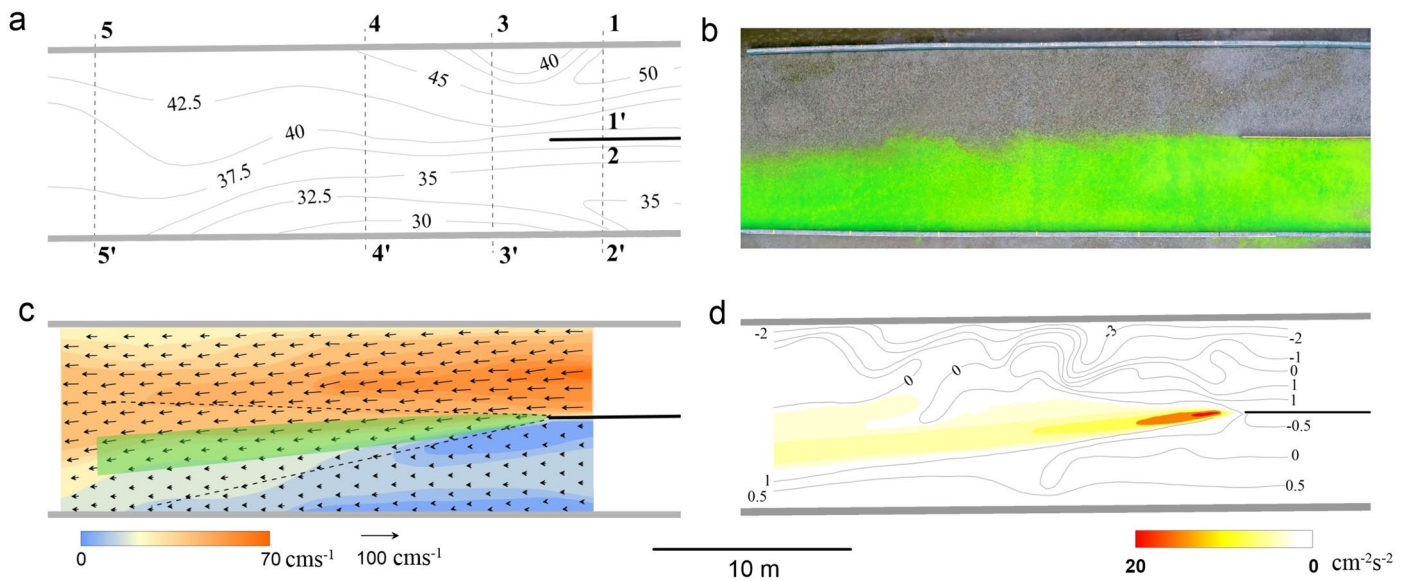
**Extended data** is available for this paper at <https://doi.org/10.1038/s41561-022-01091-1>.

**Supplementary information** The online version contains supplementary material available at <https://doi.org/10.1038/s41561-022-01091-1>.

**Correspondence and requests for materials** should be addressed to A. N. Sukhodolov.

**Peer review information** *Nature Geoscience* thanks Chris Paola and Saiyu Yuan for their contribution to the peer review of this work. Primary Handling Editor: Tamara Goldin, in collaboration with the *Nature Geoscience* team.

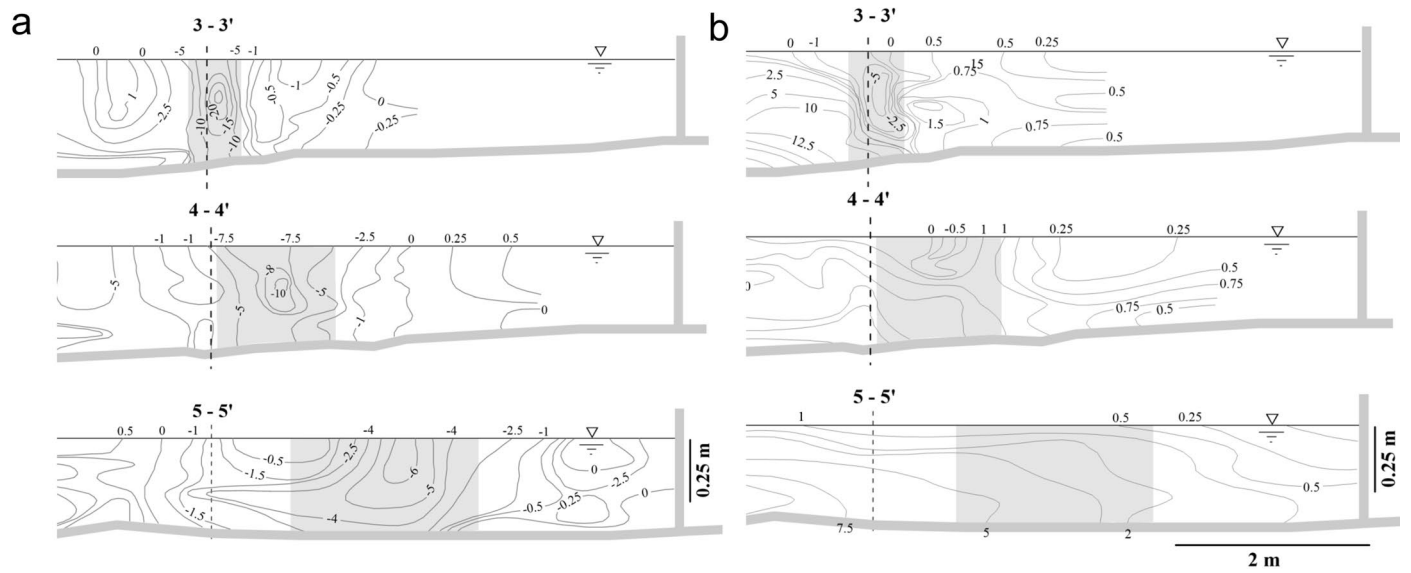
**Reprints and permissions information** is available at [www.nature.com/reprints](http://www.nature.com/reprints).



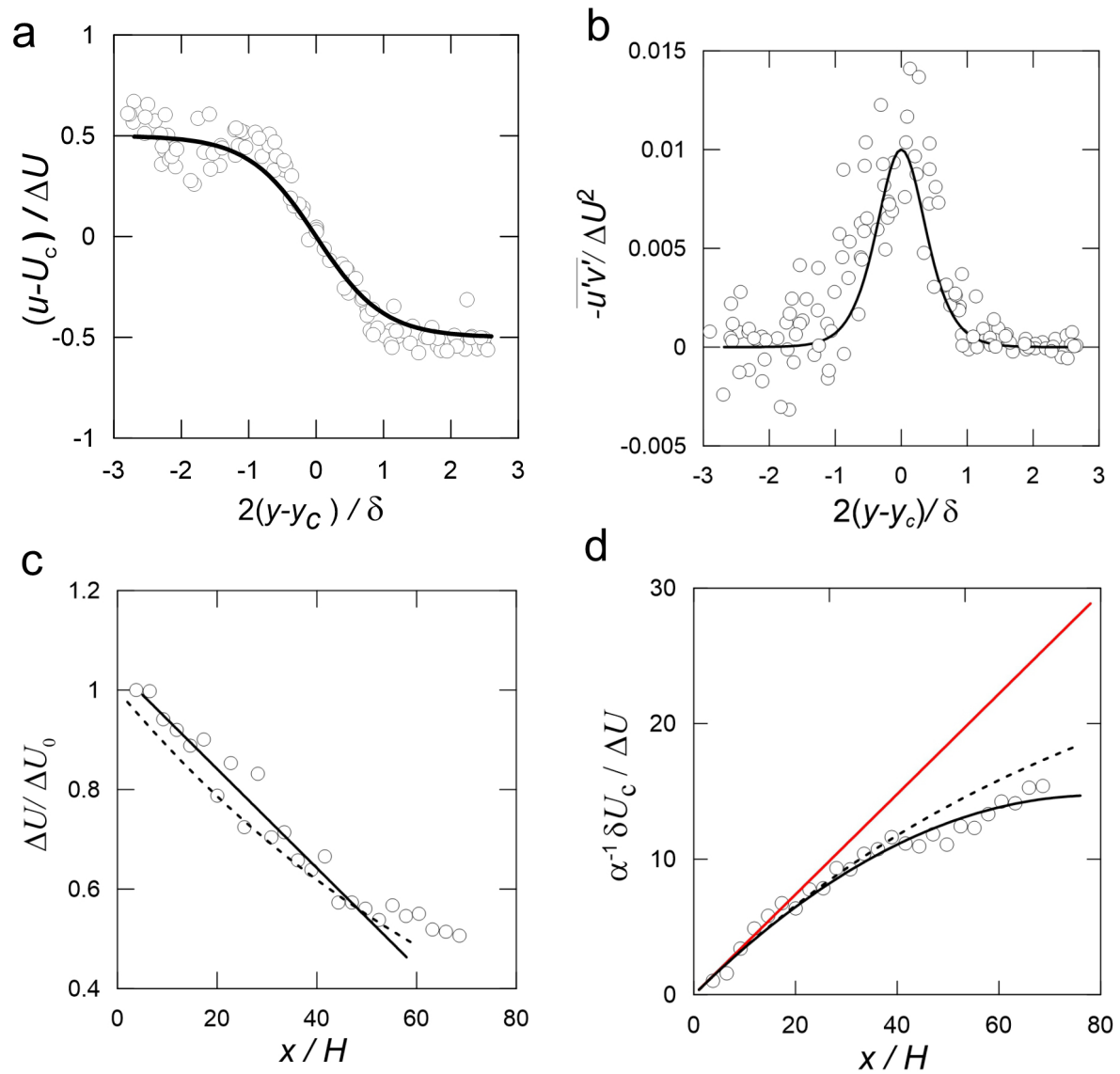
**Extended Data Fig. 1 | Experimental setup with a shallow mixing layer model,  $M_r = 20$ .** **a**, Bathymetry (contour depth in cm, dashed lines indicate cross-sections). **b**, Visualization with a solution of uranine dye. **c**, Time-averaged velocity patterns at the mid-depth plane (color contours are velocity

magnitudes, green shading highlights the area of the shallow mixing layer, and dashed lines indicate the boundaries of a free mixing layer). **d**, Pattern of lateral turbulent fluxes of momentum  $-\overline{uv}$  measured at the mid-depth plane (contour lines are fluxes with small values).



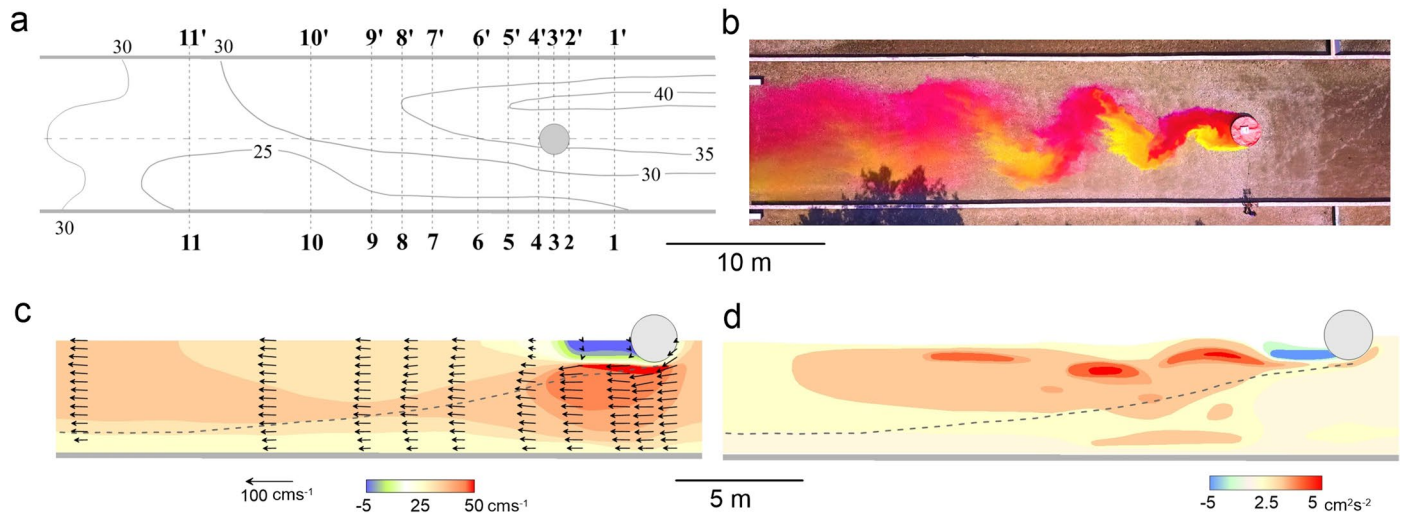


**Extended Data Fig. 2 | Patterns of turbulent fluxes of momentum in a shallow mixing layer,  $M_r = 20$ .** **a**, Lateral turbulent fluxes of momentum  $-\overline{u'v'}$ . **b**, Vertical turbulent fluxes of momentum  $-\overline{u'w'}$ . Contour lines are in  $\text{cm}^2\text{s}^{-2}$ ; and grey shading highlights the mixing layer area; dashed lines show positions of the flume centerline, locations of the sections are shown on Extended Data Fig. 1a.



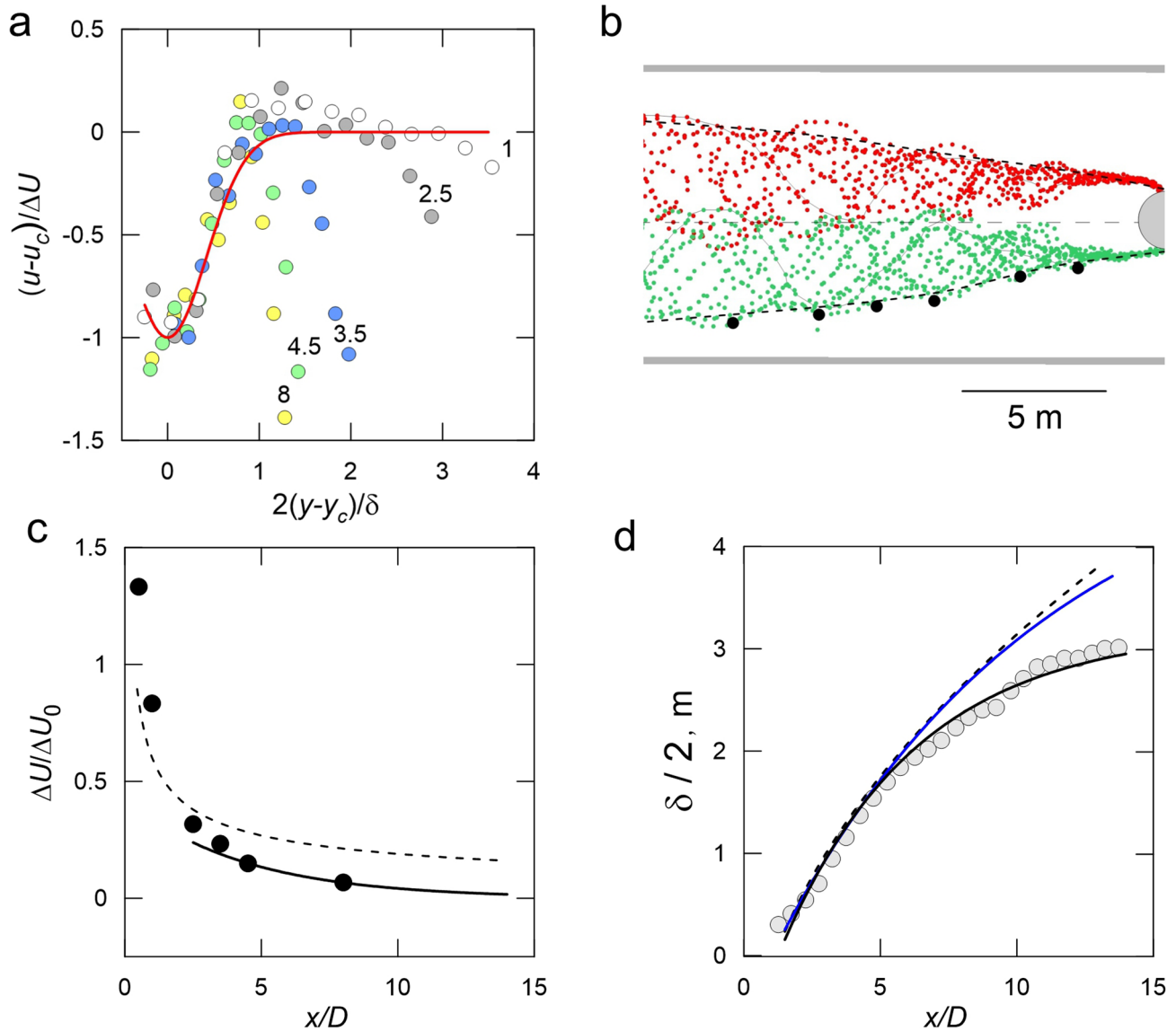
**Extended Data Fig. 3 | Normalized characteristics of the shallow mixing layer,  $M_r = 20$ .** **a**, Lateral profile of mean streamwise velocity in the mid-depth plane (solid line is hyperbolic tangent function<sup>37</sup>). **b**, Lateral profile of turbulent lateral fluxes of momentum (solid line is the hyperbolic squared cosign function<sup>36</sup>).

**c**, Velocity difference along the shallow mixing layer (solid line is Eq. (2) and dashed line is Eq. (3)). **d**, Width of the shallow mixing layer (solid red line is the free mixing layer, solid black line is Eq. (6), dashed line is Eq. (7)).



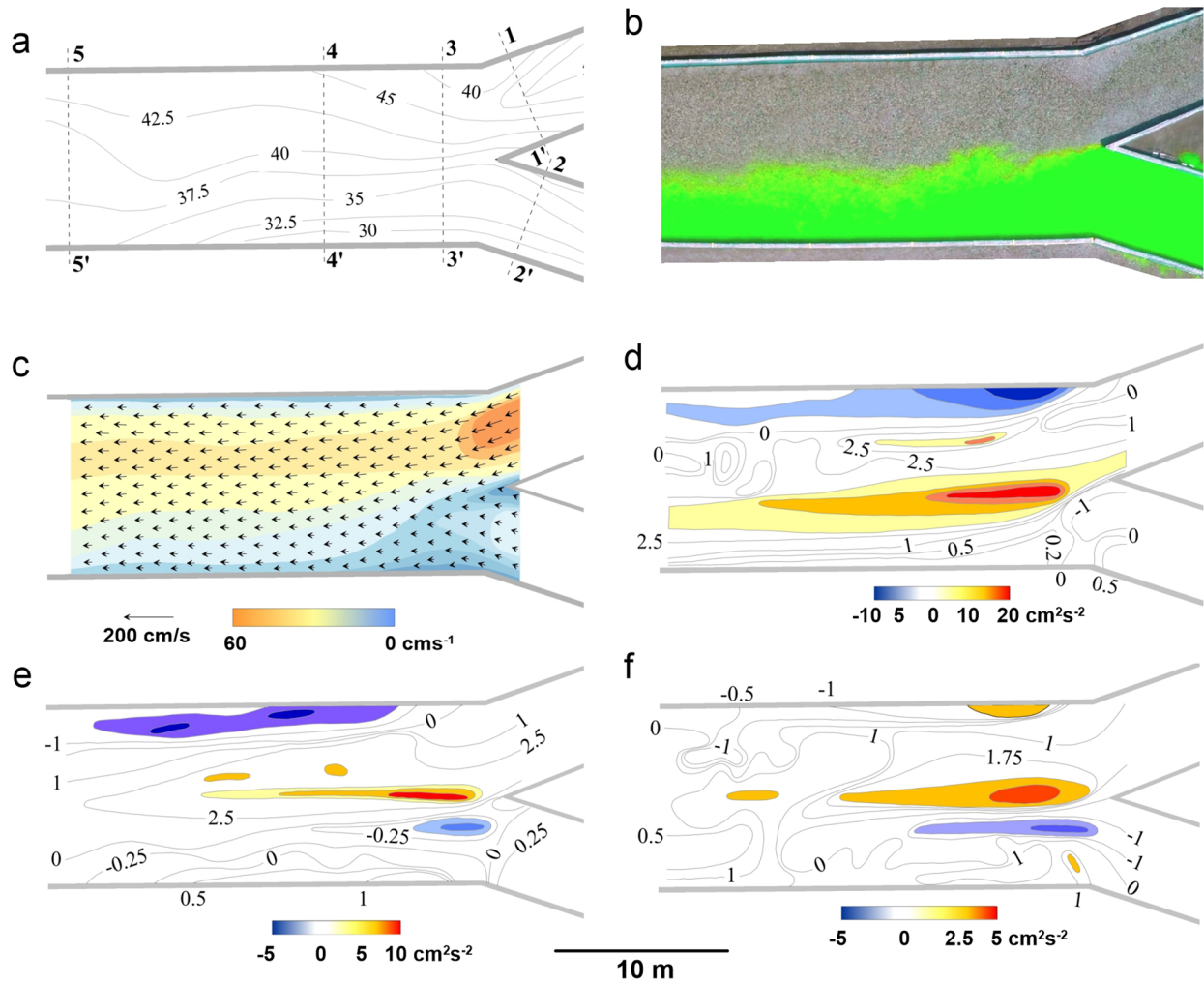
**Extended Data Fig. 4 | Experimental setup with a shallow wake model produced by a circular emerging obstruction,  $D = 2$ ,  $U_0 = 0.31 \text{ ms}^{-1}$ .**  
**a**, Bathymetry (contour depth in cm, dashed lines show positions of cross-sections, grey circle is the obstruction). **b**, Visualization with the solutions of uranine (yellow) and rhodamine (red) dyes. **c**, Time-averaged velocity patterns at

the mid-depth plane (color contours are velocity magnitudes and dashed line indicates the boundary of the wake). **d**, Pattern of lateral turbulent fluxes of momentum  $-\overline{uv}$  measured at the mid-depth plane (dashed line indicates the boundary of the wake).



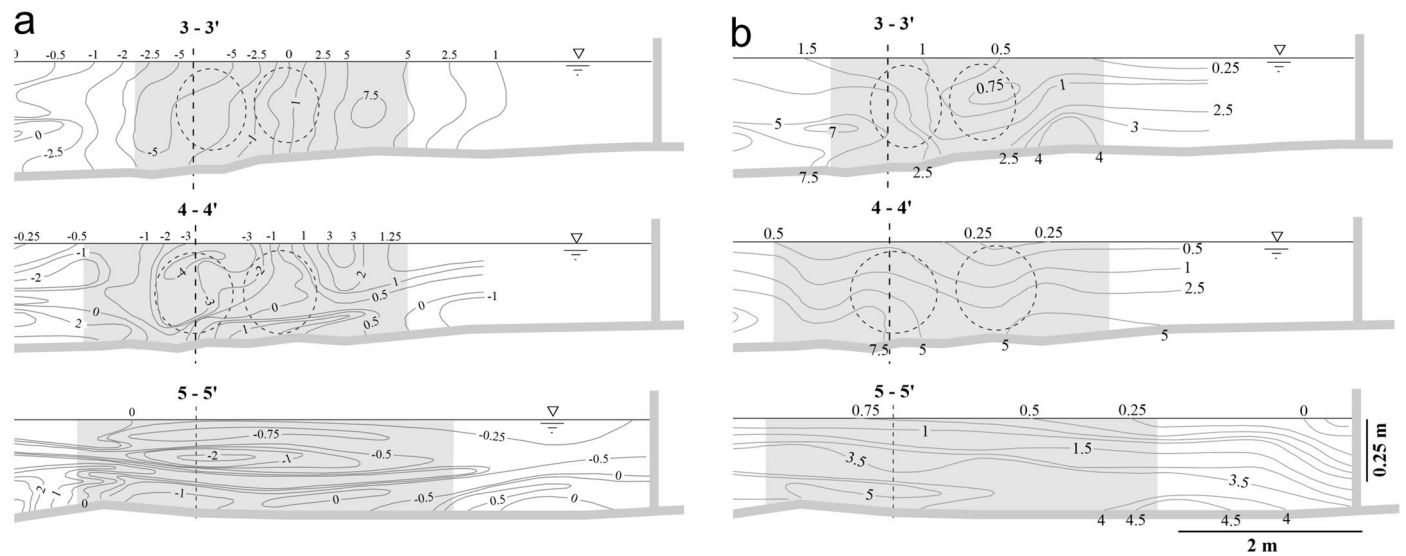
**Extended Data Fig. 5 | Normalized characteristics of the shallow wake,  $D = 2$ ,  $U_0 = 0.31 \text{ ms}^{-1}$ .** **a**, Lateral profiles of streamwise velocity (color coding shows  $x/D$ ). **b**, Ensemble of instantaneous locations of outer boundaries from flow visualizations (left (green), right (red) boundaries and wake half width from velocity profiles (black dots)). **c**, Velocity difference dynamics (symbols

are measured values, solid red line is the best fit of Eq. (3), and dashed line is a free wake). **d**, Wake half width dynamics (dashed line is free wake, blue line is Eq. (7) based on bed friction alone, and black line is Eq. (7) with the total flux of momentum).



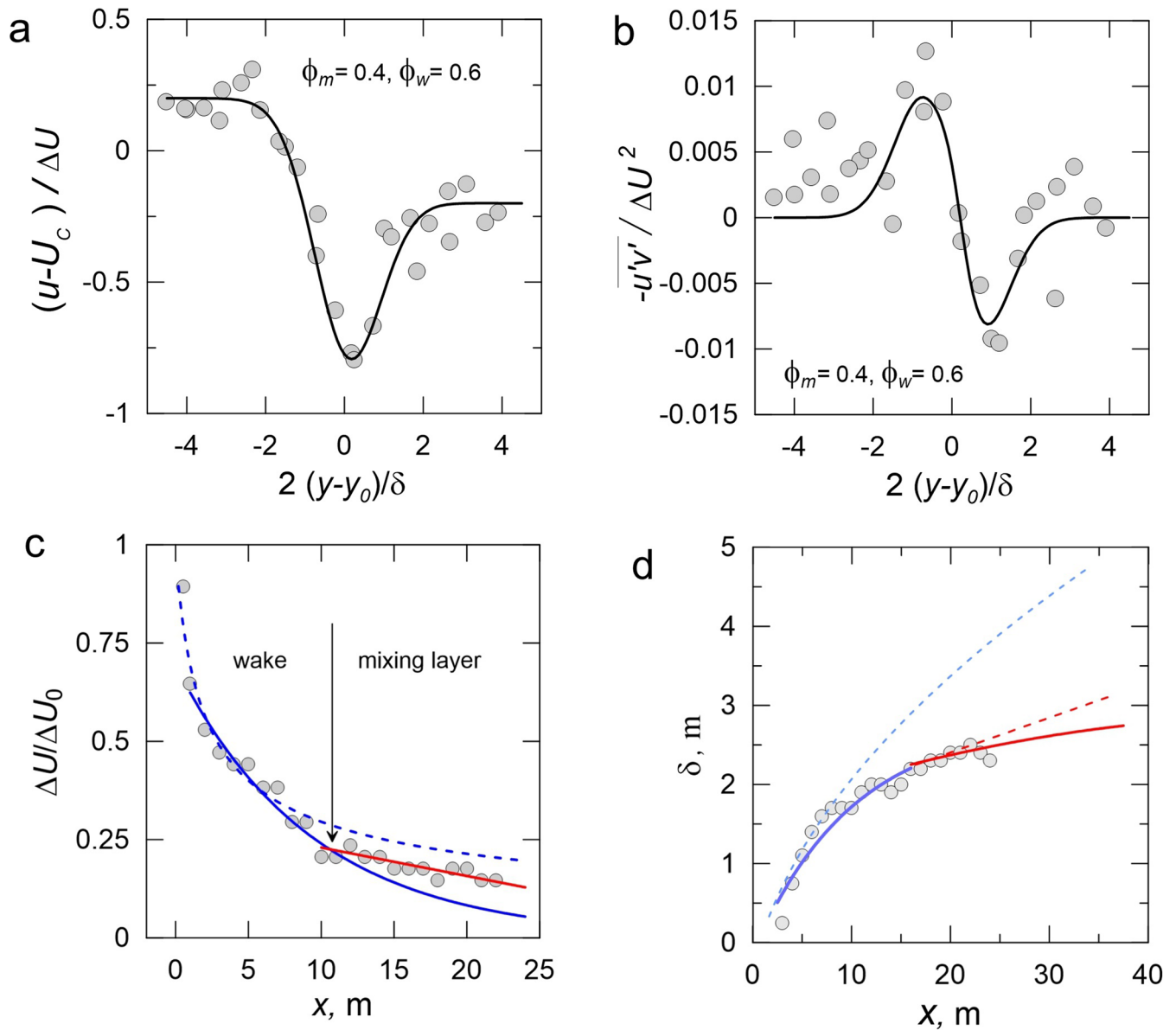
**Extended Data Fig. 6 | Results of field-based experiments with 40° confluence.** **a**, Bathymetry (contour depth in cm) of the confluence model (dashed lines show positions of representative cross-sections). **b**, Visualization with a solution of uranine dye ( $M_r = 2.2$ ). **c**, Time-averaged velocity patterns at the

mid-depth plane ( $M_r = 50$ , color contours are velocity magnitudes). **d-f**, Patterns of lateral turbulent fluxes of momentum  $-\overline{u'v'}$  at the mid-depth plane (**d**,  $M_r = 50$ ; **e**,  $M_r = 5.9$ ; and **f**,  $M_r = 2.2$ ).



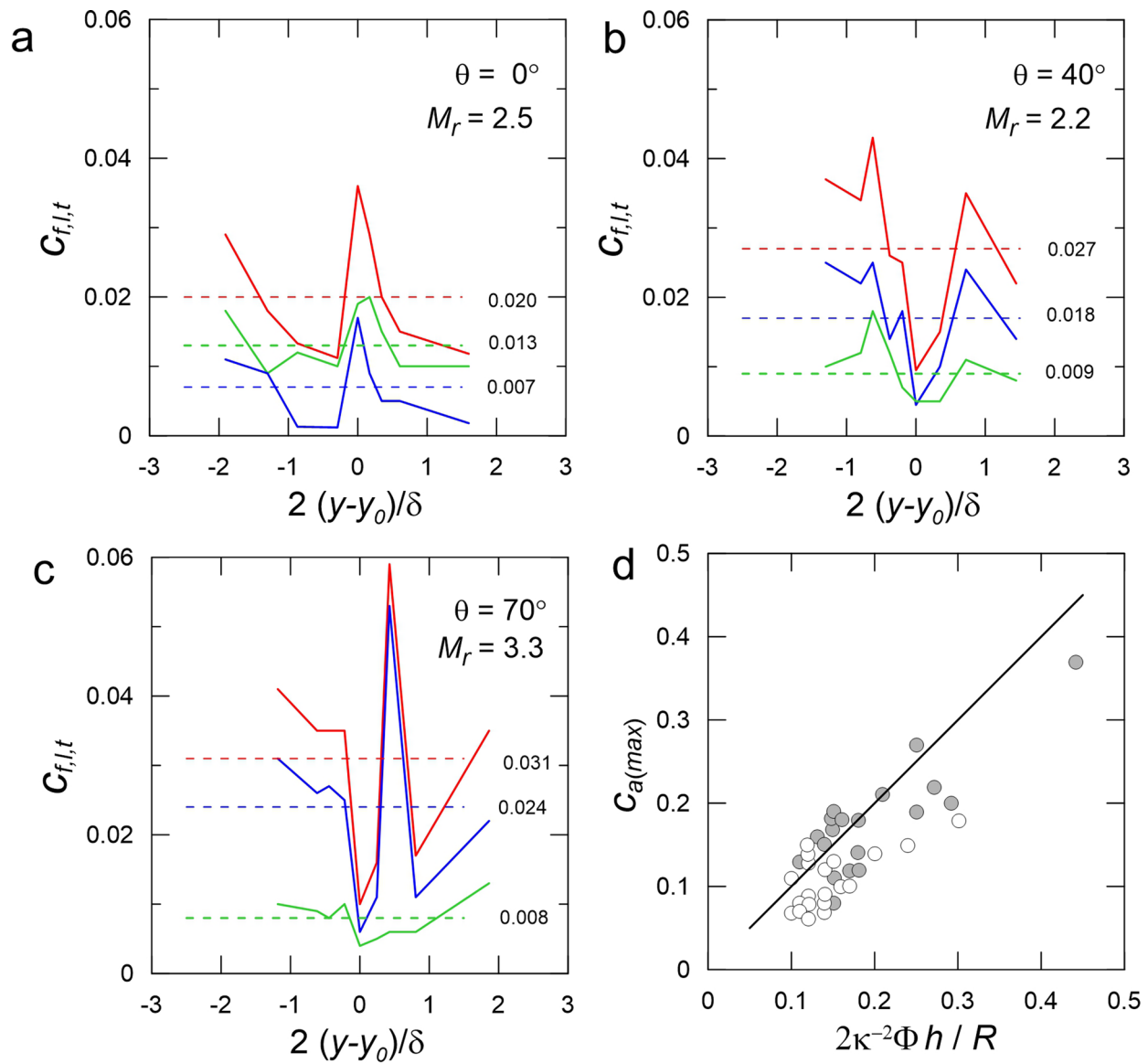
**Extended Data Fig. 7 | Patterns of turbulent fluxes of momentum in the experiments with 40° confluence,  $M_r = 2.2$ .** **a**, lateral turbulent fluxes of momentum  $-\overline{u'v'}$ . **b**, vertical turbulent fluxes of momentum  $-\overline{u'w'}$ . Contour

lines are in  $\text{cm}^2/\text{s}^2$ ; grey shading highlights the area of mixing interface; dashed straight lines show positions of the centerline; and dashed ellipses indicate the SOV cells.



**Extended Data Fig. 8 | Intermodal behavior of the mixing interface in 40° confluence model,  $M_f = 2.2$ .** **a**, Normalized lateral streamwise velocity profiles across the mixing interface at  $x < 10$  m (solid line is Eq. (8)). **b**, Lateral turbulent fluxes of momentum  $-\overline{u'v'}$  across the mixing interface at  $x < 10$  m (solid line is

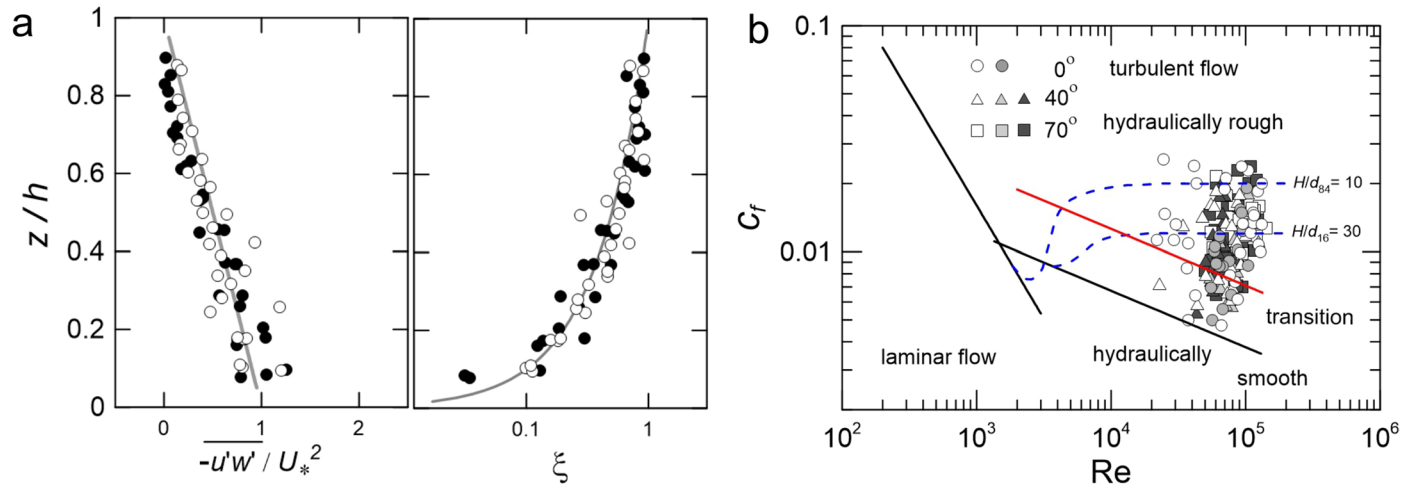
Eq. (S16)). **c**, Velocity difference along the mixing interface (dashed line is the free wake; solid blue line is Eq. (3); red line is Eq. (2)). **d**, Width of the mixing interface (dashed blue line is free wake, dashed red line is free mixing layer, red line is Eq. (6), and blue line is Eq. (7)).



**Extended Data Fig. 9 | Components of flow resistance and comparison of predicted and measured maximum values of lateral advective fluxes of momentum.** Contribution of lateral advective and turbulent fluxes of momentum  $c_l$  (blue lines) and bed friction  $c_f$  (green lines) to the total resistance

factor  $c_t$  (red lines) as a functions of junction angle of a confluence (cross-sections 3-3' Extended Data Fig. 1 and 6), d. Measured maximum lateral advective fluxes of momentum versus predicted (open symbols for  $\Phi (\eta = 0.8)$  and closed symbols for  $\Phi (\eta = 0.1)$ ).





**Extended Data Fig. 10 | Vertical structure of the flow and bed friction.** **a**, Normalized profiles of vertical turbulent fluxes of momentum (left panel, solid line is Eq. (S17)) and streamwise velocity (right panel, solid line is Eq (S18) scaled as Eq. (S19)). **b**, Relation of bed friction factor to Reynolds number and

bed roughness parameter in the field experiments (solid black lines show bed friction in laminar and hydraulically smooth turbulent flows, dashed blue lines are hydraulically rough turbulent flows and the red line indicates transition from hydraulically smooth to hydraulically rough flow).